

# Gradient-based Feature Extraction From Raw Bayer Pattern Images

Wei Zhou, *Student Member, IEEE*, Ling Zhang, Shengyu Gao and Xin Lou, *Member, IEEE*

**Abstract**—In this paper, the impact of demosaicing on gradient extraction is studied and a gradient-based feature extraction pipeline based on raw Bayer pattern images is proposed. It is shown both theoretically and experimentally that the Bayer pattern images are applicable to the central difference gradient-based feature extraction algorithms without performance degradation, or even with superior performance in some cases. The color difference constancy assumption, which is widely used in various demosaicing algorithms, is applied in the proposed Bayer pattern image-based gradient extraction pipeline. Experimental results show that the gradients extracted from Bayer pattern images are robust enough to be used in histogram of oriented gradients (HOG)-based pedestrian detection algorithms and shift-invariant feature transform (SIFT)-based matching algorithms. By skipping most of the steps in the image signal processing (ISP) pipeline, the computational complexity and power consumption of a computer vision system can be reduced significantly.

**Index Terms**—Gradient, Bayer pattern image, feature extraction, demosaicing

## I. INTRODUCTION

Computer vision studies how to extract useful information from digital images and videos to obtain high-level understandings. As an indispensable component, image sensors convert the outside world scene to digital images that consumed by computer vision algorithms. To produce color images, the information of three channels, i.e., red (R), green (G) and blue (B), are needed. There are two primary technology families used in today's color cameras: the mono-sensor technique and the three-sensor technique. Although three-sensor cameras are able to produce high-quality color images, their popularity is limited by the high manufacturing cost and large size [1]. As an alternative, the mono-sensor technique is employed in most of the digital color cameras and smartphones nowadays. In a mono-sensor color camera, images are captured with one sensor covered by a color filter array (CFA), e.g., the Bayer pattern [2] shown in Fig. 1(a), such that only one out of three color components is captured by each pixel element. This single channel image is converted to a color image by interpolating the other two missing color components at each pixel. This process is referred to as demosaicing, which is a fundamental step in the traditional image signal processing (ISP) pipeline. Apart from the demosaicing step, other ISP stages are usually determined by the manufactures according to the application scenarios [3].

Almost all the existing computer vision algorithms take images processed by the ISP pipeline as inputs. However, the existing ISP pipelines are designed for photography with a goal of generating high-quality images for human consumption. Although pleasing reproductions of the scenes can be produced, no additional information is put in by the ISP. In addition, it has been shown that the ISP pipeline may introduce cumulative errors and undermine the original information from image sensors [4]. For example, as the demosaicing process smoothes the image, the information entropy of the image decreases [5]. Moreover, it has been shown that ISP algorithms are computation intensive and consume a significant portion of processing time and power in a computer vision system [6], [7]. If certain ISP steps are not necessary, we can skip them to reduce the computational complexity and power consumption of the system. Therefore, for computer vision applications, the configuration or even the necessity of the complete ISP pipeline needs to be reconsidered.

The optimal configuration of the ISP pipeline for different computer vision applications remains an open problem [7]–[9]. In a recent paper, Buckler et. al. use an empirical approach to study the ISP's impact on different vision applications [7]. Extensive experiments based on eight existing vision algorithms are conducted and a minimal ISP pipeline consisting of denoise, demosaicing and gamma compression is proposed. But all the conclusions in [7] are drawn based on experimental results without detailed theoretical analysis. There are also some studies that try to bypass the traditional ISP and extract the high-level global features such as edge and local binary pattern (LBP), from Bayer pattern images [10]–[12]. Moreover, it is experimentally shown in [13] and [14] that the Bayer pattern images can be applied directly in some local feature descriptors such as scale-invariant feature transform (SIFT) and speeded up robust features (SURF) with negligible performance degradation.

It is noted that all the aforementioned works are experiment based, such that the applicability of their results to other vision algorithms is unclear. In this paper, the impact of demosaicing on gradient-based feature extraction is studied. It is shown both theoretically and experimentally that the raw Bayer pattern images are applicable to the central difference gradient-based feature extraction algorithms without performance degradation, or even with superior performance in some cases. Therefore, instead of demosaicing the Bayer pattern images before gradient computation, we propose to extract gradients directly from the Bayer pattern images by taking advantage of the color difference constancy assumption, which is widely used in demosaicing algorithms.

The authors are with the School of Information Science and Technology, ShanghaiTech University, Shanghai, China, E-mail: {zhouwei1, zhangling, gaoshy, louxin}@shanghaitech.edu.cn.

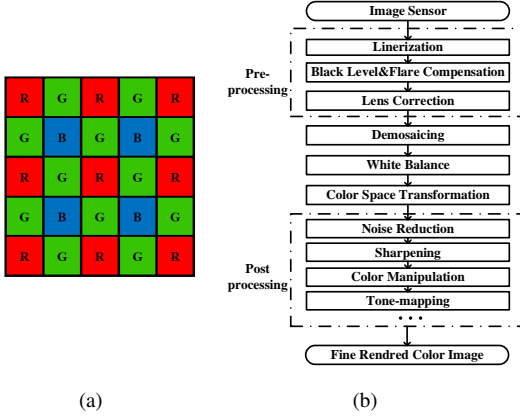


Fig. 1. (a) The RGGB Bayer CFA pattern. (b) The conventional ISP pipeline.

The remaining of the paper is organized as follows. Section II discusses the backgrounds, including the ISP pipeline and several gradient-based high-level vision features. Section III presents the derivation of the gradient-based feature extraction from the Bayer pattern images. Experimental results are presented in Section IV followed by the discussion in Section V and conclusion in Section VI.

## II. BACKGROUND

### A. The Conventional ISP Pipeline

Shown in Fig. 1(b) is an ISP pipeline from Adobe DNG converter [15]. Although the specific algorithms and their orders may vary for different manufactures, the basic steps in Fig. 1(b) are usually covered. The details of the functionality of each step is illustrated in Table I.

### B. Demosaicing

Demosaicing is a crucial step to convert a single-channel Bayer pattern image to a three-channel color image by interpolating the other two missing color components at each pixel. It has a decisive effect on the final image quality. In order to minimize the color artifacts, sophisticated demosaicing algorithms are always computation hungry.

The problem of demosaicing a Bayer pattern image has been intensively studied in the past decades and a lot of algorithms have been proposed [16]–[19]. All these algorithms can be grouped into two categories. The first category considers only the spatial correlation of the pixels and interpolates the missing color components separately using the same color channel. Although these single-channel interpolation algorithms may achieve fairly good results in the low frequency (smooth) regions, they always fail in the high-frequency regions, especially in the areas with rich texture information or along the edges [1].

To improve the demosaicing performance, the other category of algorithms takes the nature images' high spectral inter-channel correlation into account. Almost all these algorithms are based on either the color ratio constancy assumption [18] or the color difference constancy assumption [19]. According

TABLE I  
THE FUNCTIONALITIES OF THE STEPS IN ISP PIPELINE

ISP Steps	Functionality
Linerization	To transform the raw data into linear space.
Black Level & Flare Compensation	To compensate the noises contributed by black level current and flare.
Lens Correction	To compensate lens distortion and uneven light fall.
Demosaicking	To convert a single-channel Bayer pattern image a three-channel color image.
White Balance	To remove unrealistic color casts such that white objects are rendered white.
Color Space Transformation	To transform the camera color space to a standard color space.
Noise Reduction	To suppress noises introduced in preceding steps.
Sharpening	To enhance the edges for clarity improvement.
Color Manipulation	To generate different styles of photos.
Tone-mapping	To compress the dynamic range of images while preserving the visual effect.

to the Lambertian non-flat surface patches model, the three color channels can be expressed as

$$I^k(x, y) = \rho_k(x, y) \langle \vec{N}(x, y), \vec{l} \rangle, \quad (1)$$

where  $\rho$  is the reflection coefficient,  $\vec{N}(x, y)$  is the surface's normal vector at location  $(x, y)$ ,  $\vec{l}$  is the incident light vector and  $k \subseteq \{R, G, B\}$  indicates one of the three channels. At a given pixel location, the ratio of any two color components, denoted by  $k$  and  $k'$ , is given by

$$\frac{I^k(x, y)}{I^{k'}(x, y)} = \frac{\rho_k(x, y) \langle \vec{N}(x, y), \vec{l} \rangle}{\rho_{k'}(x, y) \langle \vec{N}(x, y), \vec{l} \rangle} = \frac{\rho_k(x, y)}{\rho_{k'}(x, y)}. \quad (2)$$

Suppose that objects are made up of one single material, i.e., the reflection coefficient  $\rho$  for a given channel is a constant, the ratio of  $\rho_k(x, y) / \rho_{k'}(x, y)$  reduces to a constant, such that (2) can be simplified as

$$\frac{I^k(x, y)}{I^{k'}(x, y)} = \text{constant}. \quad (3)$$

Equation (3) is referred to as color ratio constancy. Following the same manner, the color difference constancy assumption is given by

$$\begin{aligned} & I^k(x, y) - I^{k'}(x, y) \\ &= \rho_k(x, y) \langle \vec{N}(x, y), \vec{l} \rangle - \rho_{k'}(x, y) \langle \vec{N}(x, y), \vec{l} \rangle \\ &= [\rho_k(x, y) - \rho_{k'}(x, y)] \times \langle \vec{N}(x, y), \vec{l} \rangle \\ &= C(x, y). \end{aligned} \quad (4)$$

Note that the direction and amplitude of the incident light are assumed to be locally constant, such that the color component difference  $C(x, y)$  is also a constant within a neighborhood of  $(x, y)$  [1].

The color ratio and difference constancy assumptions are widely used in various demosaicing algorithms [20]. In practical applications, the color difference constancy assumption always is preferred due to its superior peak signal to noise

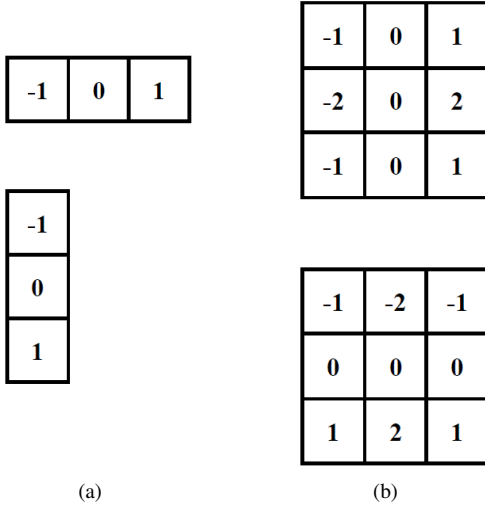


Fig. 2. Gradient operators. (a) The central difference operator and (b) the Sobel operator.

ratio (PSNR) performance. As will be shown, in this work, the color difference constancy can be utilized to directly extract the gradient information from the Bayer pattern images.

### C. High-level Features

In the past decades, many different feature descriptors such as Harr-like features [21], LBP [22], SIFT [23] and histograms of oriented gradients (HOG) [24] have been proposed for object detection. In this work, we mainly focus on the central difference gradient-based feature descriptors, study their applicability on Bayer pattern images and analyze the corresponding performances. Without loss of generality, HOG and SIFT are taken as examples in the analysis and experiments. The results can be extended to other descriptors, such as SURF [25], Color-SIFT [26], Affine-SIFT [27] and F-HOG [28], as long as the central difference is used for gradient computation.

SIFT is a local feature descriptor which detects key points in images. The computation of SIFT can be divided into five steps [29] as

- 1) Scale space construction. The scale space is approximated by the difference-of-Gaussian (DoG) pyramid, which is computed as

$$\begin{aligned} D(x, y, \sigma_i) &= (G(x, y, k^i \sigma) - G(x, y, k^{i-1} \sigma)) * I(x, y) \\ &= L(x, y, k^i \sigma) - L(x, y, k^{i-1} \sigma). \end{aligned} \quad (5)$$

Here  $G(x, y, \sigma)$  is the Gaussian function,  $k$  is a constant multiplicative factor which is determined by the number of scales  $s$  and  $*$  denotes the convolution operator.

- 2) Extremum detection. To detect the local maxima and minima by comparing each pixel with its neighbors in a  $3 \times 3$  neighbourhood among the current scale, scale above and scale below.
- 3) Key point localization. To perform a refinement of key point candidates identified in the previous step. The

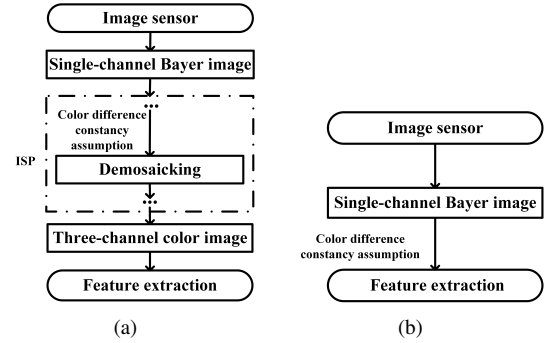


Fig. 3. Feature extraction pipelines. (a) The conventional pipeline. (b) The proposed pipeline.

unstable key points such as points with low contrast or poorly localized along an edge are rejected.

- 4) Orientation determination. To assign one or more orientations to each key point. A histogram is created for a region centered on the key point with radius of  $3\sigma_0$ , where  $\sigma_0$  is 1.5 times that of the scale of the key point. The direction with the highest bar in the histogram is regarded as the dominant direction and directions with heights of larger than 80% of the highest bar is regarded as the auxiliary directions.
- 5) Key point description. To construct a descriptor vector for each key point. A gradient histogram with 8 bins is created for each  $16 \times 16$  pixel region around the key point. The key point descriptor is constructed by concatenating the histograms of a set of  $4 \times 4$  regions around the key point.

HOG is a feature descriptor initially proposed for pedestrian detection [24]. It counts the number of occurrences of gradient orientation in a detection window. The key steps of HOG feature generation are similar to steps 4 and 5 in the SIFT descriptor. The main difference is that orientation histograms in HOG are usually computed on an  $8 \times 8$  cell and summarized as a global feature by a sliding window.

## III. GRADIENT AND MULTISCALE MODELS FOR BAYER PATTERN IMAGES

### A. Gradient Extraction from Bayer Pattern Images

Image gradient measures the change of intensity in specific directions. Mathematically, for a two-dimensional function  $f(x, y)$ , the gradients can be computed by the derivatives with respect to  $x$  and  $y$ . For a digital image where  $x$  and  $y$  are discrete values, the derivatives can be approximated by finite differences.

There are different ways to define the difference of a digital image, as long as the following three conditions are satisfied: (i) zero in constant intensity area; (ii) non-zero along the ramps and (iii) nonzero at the onset of an intensity step or ramp [30]. One of the most commonly used image gradient computation is the central difference based approach as

$$G_x = I(x+1, y) - I(x-1, y), \quad (6)$$

$$G_y = I(x, y+1) - I(x, y-1). \quad (7)$$

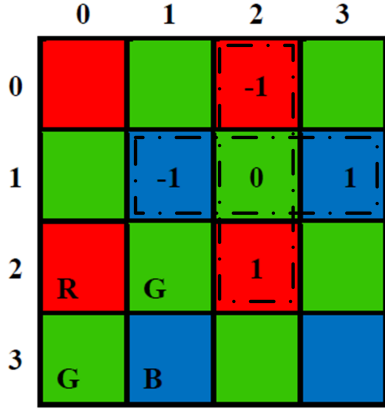


Fig. 4. Gradient computation based on Bayer pattern image. Here  $I(x, y)$  is the intensity at location  $(x, y)$ ,  $G_x$  and  $G_y$  represent the gradients in the horizontal and vertical directions, respectively. The computation of (6) and (7) can be implemented by the convolution of the templates in Fig. 2(a) with the images.

The fundamental idea of the proposed Bayer pattern image based gradient extraction is illustrated in Fig. 3(b). Instead of demosaicing the Bayer pattern images before difference computation as shown in Fig. 3(a), we propose to take advantage of the color difference constancy assumption directly for gradient extraction based on Bayer pattern images. Note that by convolving the filter templates in Fig. 2(a) directly with a Bayer pattern image, all the three conditions for a valid difference definition mentioned are satisfied. To illustrate this, let us consider the example in Fig. 4.

As we can see, the two input pixels for coefficients 1 and -1 in the convolution templates are from the same channel, i.e., differences are always computed on homogeneous pixels. As shown in Fig. 4, applying the convolution templates at locations (1, 2) generates

$$G_{x(1,2)}^B = I_{(1,3)}^B - I_{(1,1)}^B, \quad (8)$$

$$G_{y(1,2)}^R = I_{(2,2)}^R - I_{(0,2)}^R, \quad (9)$$

where  $G^B$  and  $G^R$  are the gradients of the blue and red channels, respectively.

In the demosaicing tasks, it is a common practice to interpolate the G channel first followed by the R/B channels. This is because there are twice as many G channel pixels as R/B channel pixels in Bayer pattern images. The color difference constancy assumption in (10) can then be used to estimate the missing pixels of the R and B channels.

$$I^G(x, y) = I^k(x, y) + C^k(x, y). \quad (10)$$

Here,  $k$  represents either R or B channel,  $C^k(x, y)$  is the difference between the R/B channel and the G channel at pixel location  $(x, y)$ , which needs to be estimated in demosaicing tasks [31].

Consider two pixels within a small neighborhood at locations  $(x, y)$  and  $(x', y')$ , according to (10), we have

$$\begin{aligned} & I^G(x, y) - I^G(x', y') \\ &= I^k(x, y) - I^k(x', y') + C^k(x, y) - C^k(x', y') \quad (11) \\ &= I^k(x, y) - I^k(x', y') + \delta(x, y, x', y'). \end{aligned}$$

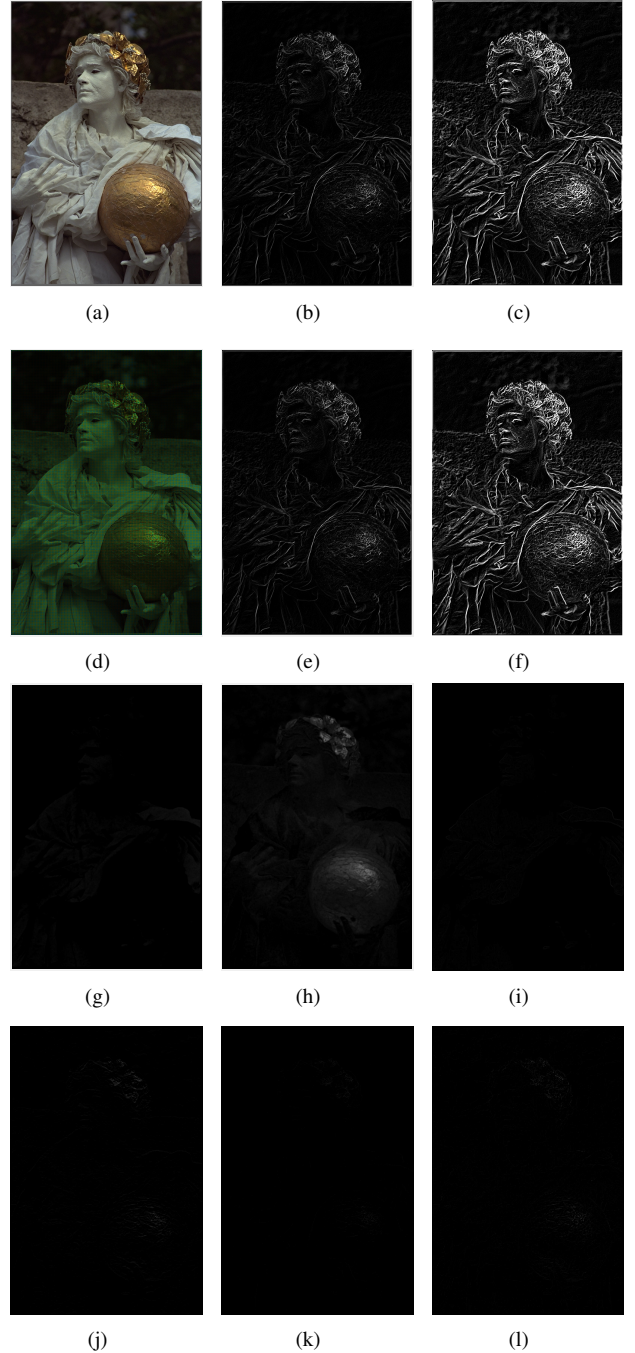


Fig. 5. Comparison of gradients extracted from a color image and its Bayer version. (a) Image Kodim17. (b)-(c): Gradient magnitude maps generated from (a) using the central difference operator and the Sobel operator in Fig. 2.(d) The resampled Bayer version of Kodim17 (displayed as a three-channel image). (e)-(f): Gradient magnitude maps generated from (d) using the central difference operator and the Sobel operator in Fig. 2. (g)-(h): The difference images of (G channel - R channel) and (G channel - B channel). (i)-(j) Gradient magnitude maps generated from (g) and (h) using operators in Fig. 2(a). (k) The difference map between (b) and (e). (l) The difference map between (c) and (f).

Where  $\delta(x, y, x', y') = C^k(x, y) - C^k(x', y')$ . The value of  $\delta(x, y, x', y')$  is crucial in our analysis and will be discussed in detail.

Generally, there are flatten areas (e.g. background) and texture areas (e.g., corners and edges) in a natural image, these two situations will be discussed separately.

For the flatten areas, the difference between two pixels is negligible such that

$$I^G(x, y) - I^G(x', y') = I^k(x, y) - I^k(x', y') \approx 0, \quad (12)$$

i.e.,  $\delta(x, y, x', y') \approx 0$ .

For the texture areas, the analysis is more complex. To analyze the areas with complex textures, (11) can be further rewritten as

$$\delta(x, y, x', y') = (I^G(x, y) - I^k(x, y)) - (I^G(x', y') - I^k(x', y')). \quad (13)$$

Note that image's gradients are always computed among a small neighborhood. Considering the central difference-based horizontal gradient computation at pixel location  $(x, y)$ , we have

$$\begin{aligned} & \delta(x+1, y, x-1, y) \\ &= (I^G(x+1, y) - I^k(x+1, y)) - (I^G(x-1, y) - I^k(x-1, y)) \\ &= I^{G-k}(x+1, y) - I^{G-k}(x-1, y) \\ &= G_x^{G-k}(x, y). \end{aligned} \quad (14)$$

Here,  $G-k$  represents the difference image of the G channel and the R/B channel. It can be observed from (14) that  $\delta(x+1, y, x-1, y)$  is exactly the gradient of the difference image at location  $(x, y)$ . It has been shown in [32] that the difference images are slowly-varying over a spatial domain, meaning that the gradient  $G_x^{G-k}(x, y)$  in (14) is negligible, i.e.,  $\delta(x+1, y, x-1, y)$  approximates to zero. Illustrated in Fig. 5(i) and Fig. 5(j) are the gradient magnitude maps of two difference maps in Fig. 5(g) and Fig. 5(h). As we can see, Fig. 5(i) and Fig. 5(j) are almost all black, except a few small areas. Therefore, for natural images,  $\delta(x, y, x', y')$  can be ignored if pixel locations  $(x, y)$  and  $(x', y')$  are within a small neighborhood.

As a result of the above discussion, (11) can be rewritten as

$$I^G(x, y) - I^G(x', y') \approx I^R(x, y) - I^R(x', y'), \quad (15)$$

$$I^G(x, y) - I^G(x', y') \approx I^B(x, y) - I^B(x', y'). \quad (16)$$

Combining the gradient definition of (6) and (7) with (15) and (16), we have

$$G \approx G^G \approx G^R \approx G^B, \quad (17)$$

meaning that the gradients of natural images can be computed using any one of the three channels as long as the color difference constancy holds. Combining (17) with (8) and (9), we have

$$G_{x(1,2)} = G_{x(1,2)}^B = I_{(1,3)}^B - I_{(1,1)}^B, \quad (18)$$

$$G_{y(1,2)} = G_{x(1,2)}^R = I_{(2,2)}^R - I_{(0,2)}^R. \quad (19)$$

Therefore, even though two color components are missing at each pixel, the gradients of location (1, 2) can be computed directly from the Bayer pattern image using the blue and red channel. The gradients of any other pixel locations can be computed in the same manner.

Generally, the above conclusion can be extended to other symmetrical first-order differential operators (with alternating zero and nonzero coefficients) on any kind of Bayer pattern. Let us take the Sobel operators in Fig. 2(b) as an example. Applying the Sobel operators in Fig. 2(b) to the pixel location (1, 2) of the Bayer pattern image results

$$\begin{aligned} G'_{x(1,2)} &= I_{(0,3)}^G + 2 \times I_{(1,3)}^B + I_{(2,3)}^G - I_{(0,1)}^G - 2 \times I_{(1,1)}^B - I_{(2,1)}^B \\ &= (I_{(0,3)}^G - I_{(0,1)}^G) + 2 \times (I_{(1,3)}^B - I_{(1,1)}^B) + (I_{(2,3)}^G - I_{(2,1)}^G), \end{aligned} \quad (20)$$

$$\begin{aligned} G'_{y(1,2)} &= I_{(2,1)}^G + 2 \times I_{(2,2)}^R + I_{(2,3)}^G - I_{(0,1)}^G - 2 \times I_{(0,2)}^R - I_{(0,3)}^G \\ &= (I_{(2,1)}^G - I_{(0,1)}^G) + 2 \times (I_{(2,2)}^R - I_{(0,2)}^R) + (I_{(2,3)}^G - I_{(0,3)}^G). \end{aligned} \quad (21)$$

As for gradient computation using (6) and (7), differences are always computed on homogeneous pixels for Sobel-based differential operations. Moreover, according to the color difference constancy assumption, (20) and (21) can be rewritten as

$$\begin{aligned} G'_{x(1,2)} &\approx (I_{(0,3)}^{\hat{R}} - I_{(0,1)}^{\hat{R}}) + 2 \times (I_{(1,3)}^{\hat{R}} - I_{(1,1)}^{\hat{R}}) + (I_{(2,3)}^{\hat{R}} - I_{(2,1)}^{\hat{R}}) \\ &\approx (I_{(0,3)}^{\hat{G}} - I_{(0,1)}^{\hat{G}}) + 2 \times (I_{(1,3)}^{\hat{G}} - I_{(1,1)}^{\hat{G}}) + (I_{(2,3)}^{\hat{G}} - I_{(2,1)}^{\hat{G}}) \\ &\approx (I_{(0,3)}^{\hat{B}} - I_{(0,1)}^{\hat{B}}) + 2 \times (I_{(1,3)}^{\hat{B}} - I_{(1,1)}^{\hat{B}}) + (I_{(2,3)}^{\hat{B}} - I_{(2,1)}^{\hat{B}}), \end{aligned} \quad (22)$$

$$\begin{aligned} G'_{y(1,2)} &\approx (I_{(2,1)}^{\hat{R}} - I_{(0,1)}^{\hat{R}}) + 2 \times (I_{(2,2)}^{\hat{R}} - I_{(0,2)}^{\hat{R}}) + (I_{(2,3)}^{\hat{R}} - I_{(0,3)}^{\hat{R}}) \\ &\approx (I_{(2,1)}^{\hat{G}} - I_{(0,1)}^{\hat{G}}) + 2 \times (I_{(2,2)}^{\hat{G}} - I_{(0,2)}^{\hat{G}}) + (I_{(2,3)}^{\hat{G}} - I_{(0,3)}^{\hat{G}}) \\ &\approx (I_{(2,1)}^{\hat{B}} - I_{(0,1)}^{\hat{B}}) + 2 \times (I_{(2,2)}^{\hat{B}} - I_{(0,2)}^{\hat{B}}) + (I_{(2,3)}^{\hat{B}} - I_{(0,3)}^{\hat{B}}), \end{aligned} \quad (23)$$

where  $\hat{R}$ ,  $\hat{G}$  and  $\hat{B}$  represent the missing color components at the corresponding locations. Therefore, the Sobel-based gradients can also be extracted directly from the Bayer pattern images as long as the color difference constancy holds.

In terms of different Bayer patterns, they are merely different arrangements of the RGB pixels, while the alternating pattern of  $R$ ,  $G$  and  $B$  at each row and column are preserved. For example, discarding the first column of the Bayer pattern in Fig. 4 generates the GRBG Bayer pattern. Therefore, different Bayer patterns do not have any impact on the applicability of the discussed differential operators to Bayer pattern images. Moreover, the discussed gradient extraction method can be directly extended to other CFA patterns with alternating color filter arrangements, e.g., RYYB and RGB-IR, etc.

To validate the proposed Bayer pattern image-based gradient extraction, the differential operators in Fig. 2 are applied to a true color image Kodim17 from the Kodak image dataset [33] and the corresponding resampled Bayer version. The generated gradient maps are shown in Fig. 5. For display purposes, the Bayer pattern image in Fig. 5(b) is presented as a three-channel image to illustrate its Bayer "mosaic" structure. As illustrated in Fig. 5, the gradient maps generated from the Bayer pattern images looks almost the same as that generated from the true color version. To compare these gradient maps, two difference maps, which are the results of the gradient maps from the color image minus the corresponding gradient maps

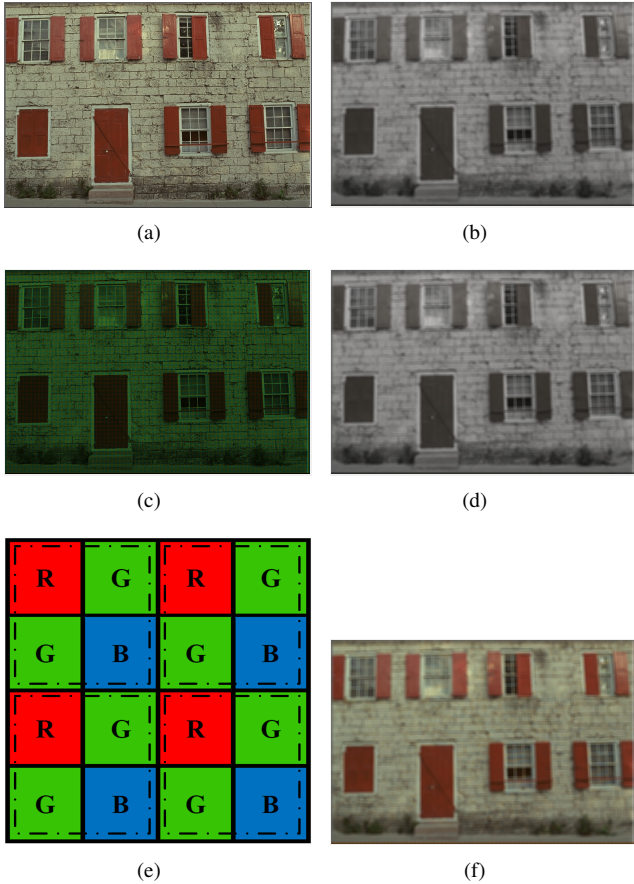


Fig. 6. (a) The true color image Image Kodim01. (b) Gaussian blurred version of (a). (c) Bayer vision of (a). (d) Direct Gaussian blurred version of (c) then demosaicing. (e) The  $2 \times 2$  super-pixel structure. (f) Super-pixel structure-based Gaussian blurred version of (c) then demosaicing.

from the Bayer pattern image, are presented. As can be seen, the two difference maps are almost pure black, which means the compared gradient maps are very close to each other.

### B. The Multiscale Model for Bayer Pattern Images

In SIFT, the scale-space is approximated by a DoG pyramid. The construction of the DoG pyramid can be divided into two parts: Gaussian blurring at different scales and resizing of the blurred images. Due to the special alternating pixel arrange of Bayer pattern images, directly Gaussian blur the images will destroy the “mosaic structure”. This phenomenon can be illustrated using Fig. 6. If the Bayer pattern image is directly Gaussian filtered, the resulting image (after demosaicing) looks like a “three-channel grayscale image” as shown in Fig. 6(d), meaning that the “mosaic structure” is destroyed and the color information of the image is lost. This is conflict with the theory of scale space that the color of an object does not change with distance or size. Moreover, lost of the color information makes some of the algorithm in the SIFT family such as C-SIFT and RGB-SIFT no longer applicable.

To address the above mentioned problem, the super-pixel approach as illustrated in Fig. 6(e) is used in this work. A super-pixel is a compound pixel consisting of a complete Bayer pattern. The Bayer pattern image can therefore be

TABLE II  
COMPARISON RESULTS OF THE TRUE COLOR IMAGES AND IMAGES GENERATED USING DIFFERENT DEMOSAICING ALGORITHMS

Methods	Average		
	MSSIM	PSNR	GMSD
Nearest neighbor	0.8865	25.744	0.082
Linear interpolation	0.945	29.255	0.089
Cubic interpolation	0.952	29.354	0.084
Adaptive color plane interpolation	0.976	34.452	0.070
Gradient-corrected linear interpolation	0.986	34.552	0.068
Hybrid interpolation	0.990	39.010	0.065

regarded as a “continuous” image filling with super-pixels. Operating on the super-pixel structure preserves the Bayer pattern of the original images. Fig. 6(f) shows the Gaussian blurred image (after demosaicing) based on the super-pixel structure. As can be seen, it is close to that generated by the full color approach. Moreover, the super-pixel structure can also be used for resize when constructing the scale space. The detailed comparison results will be presented in Section IV-C.

## IV. EXPERIMENTS

In this section, experimental results are presented to demonstrate the effectiveness of the proposed Bayer pattern image-based gradient extraction. The datasets used in the experiments are introduced first, followed by the details of the experiments setup and evaluation results.

### A. Datasets

There are five datasets used for different experiments in this work. Among these five datasets, four are commonly used benchmarks in different image processing and computer vision tasks such as demosaicing, pedestrian detection. A brief description of these datasets is presented in Table III.

### B. Experiments Setup and Evaluation Criteria

1) *Gradient Map and Multiscale Model*: In our experiment, the operators in Fig. 2(a) are used to extract the gradients from color images and their corresponding Bayer versions. For color images, gray scale images are generated for gradient extraction. To blur and resize the Bayer pattern images, the super-pixel structure discussed in Section III-B is utilized.

To estimate the differences among gradient maps, blurred images and resized images, some image quality assessment methods are used in these experiments.

The gradient magnitude similarity deviation (GMSD) is proposed in [38] to evaluate the similarity of gradient magnitudes. Given two gradient maps, the GMSD is given by

$$GMSD = \sqrt{\frac{1}{N} \sum_{i=1}^{i=N} (GMS(i) - GMSM)^2}, \quad (24)$$

where,

$$GMSM = \frac{1}{N} \sum_{i=1}^{i=N} GMS(i), \quad (25)$$

TABLE III  
NOTATION OF DIFFERENT DATASETS USED IN EXPERIMENTS.

Datasets	Brief Introduction	Generation of the Corresponding Color/Bayer Versions	
		Color	Bayer
The Kodak lossless true color image suite [33]	A popular standard test suite for demosaicing algorithms.	-	Resampling according to the corresponding Bayer pattern.
The SHTech pedestrian dataset	Our own pedestrian dataset shoot by a Huawei Honor 8 mobile phone with the FreeDcam APP [34] to by pass the entire ISP.	ISP pipeline in [15].	-
The PASCALRAW dataset [35]	A recently published raw image dataset for object detection.	ISP pipeline in [15].	-
The INRIA pedestrian dataset [36]	A popular dataset for pedestrian detection algorithms.	-	Reverse ISP pipeline introduced in [6].
The See-in-the-Dark (SID) dataset [37]	A recently published raw image dataset shoot under low light conditions.	-	-

$$GMS(i) = \frac{2m_1(i)m_2(i) + c}{m_1^2(i) + m_2^2(i) + c}. \quad (26)$$

Here,  $m_k(i)$  is the gradient magnitude of the  $k$ th image, defined by  $m = \sqrt{G_x + G_y}$  and  $c$  is a small value set to 0.0026 to avoid divisions by 0. According to [38], the smaller the GMSD is, the closer the gradient maps are.

Mean squared error (MSE) is the simplest and most commonly used full-reference quality metric. It is an evaluation that is computed by averaging the squared intensity differences of distorted and reference image pixels. For two given images, the MSE is given by

$$MSE = \frac{1}{H \times W} \sum_{x=1}^H \sum_{y=1}^W (I_1(x, y) - I_2(x, y))^2, \quad (27)$$

where  $W$  and  $H$  is the width and height of the image. The MSE can be converted to PSNR by

$$PSNR = 10 \log_{10} \left( \frac{(2^n - 1)^2}{MSE} \right), \quad (28)$$

where  $n$  represent the pixel depth of images. For images with 8-bit pixel depth, the typical values of PSNR for lossy images are between 30 and 50 dB [39].

Structural similarity (SSIM) is also a full-reference quality metric which compares luminance, contrast, structure among two images [40]. The SSIM ranges from 0 to 1, where 1 means that the two compared images are identical. Due to the fact that SSIM is a metric for local region comparison, the mean SSIM (MSSIM) is usually used in practice.

2) *Influence of Noise*: Noise reduction, which has a deterministic impact on the quality of imaging, is a critical step in image processing pipelines. Basically, there are two kinds of noise in an image, i.e., signal-independent noise (e.g., bad-pixels, dark currents) and signal-dependent noise (e.g., photonic noise). For modern cameras, the signal-dependent noise, which is affected by lighting conditions and exposure time [41], [42], is the dominant noise source. In [41], image noise is modeled as a mixture of Gaussian and Poissonian process which obeys the distribution of

$$\eta_h \sim N(0, ay(x) + b). \quad (29)$$

Here,  $\eta_h$  is the signal noise,  $y(x)$  is the noise-free signal and  $a, b$  are two parameters. Note that the dataset used in

TABLE IV  
COMPARISON RESULTS OF BAYER IMAGE BASED AND COLOR IMAGE BASED GRADIENTS

Datasets	Average		
	MSSIM	PSNR	GMSD
Kodak	0.975	38.276	0.069
SHTech	0.850	34.683	0.119
PASCALRAW	0.9367	37.36	0.127
INRIA	0.817	30.288	0.148

For the INRIA dataset, gamma compression with scale factor of 2 and exponent of 0.5 is used.

pedestrian detection experiments are all shoot under sufficient illumination and proper exposure. To study the influence of noise on the proposed Bayer pattern image-based gradient feature extraction pipeline, we use the See-in-the-Dark (SID) dataset introduced in [37] and the model in (29) to obtain a set of different noise parameters under low light conditions (2650 parameter pairs in total) and randomly choose parameter pairs for each image in pedestrian detection datasets to generate the corresponding noisy images.

3) *HOG Descriptor*: The traditional HOG+support vector machine (SVM) framework proposed in [24] is used to detect pedestrians from color images and their Bayer visions. In order to evaluate the full image performance more accurately, the experimental results are presented based on per-image criteria [43].

4) *SIFT Descriptor*: For the proposed Bayer pattern image-based SIFT feature extraction, extremums are searched among a  $5 \times 5$  neighborhood instead of  $3 \times 3$ . To validate the scale and rotation invariant property of the generated SIFT features, key points are detected from the transformed images, i.e., the resized, rotated and blurred images. These key points are matched with the ones detected from the untransformed images. The repeatability criteria introduced in [44] is used to evaluate the performance of SIFT descriptors in finding matching points. Given a pair of images, the repeatability is defined by

$$P = \frac{M(I(x_1, y_1), I(x_2, y_2))}{\min(n_1, n_2)}, \quad (30)$$

where  $n_1$  and  $n_2$  are the number of descriptors detected on the images,  $M(I(x_1, y_1), I(x_2, y_2))$  is the correct matches.

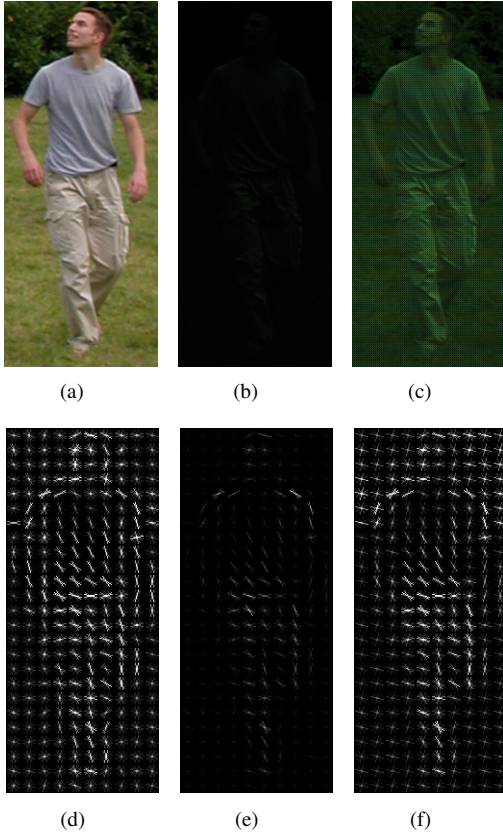


Fig. 7. Comparison of HOG features. An image from the INRIA pedestrian dataset. (b) The converted Bayer version of (a) using the reverse pipeline in [7]. (c) The Bayer version image after gamma compression. (d)-(f): Visualization of the generated HOG descriptors.

A pair of points  $I(x_1, y_1)$  and  $I_{tran}(x_2, y_2)$  is considered matched within a  $t$ -neighborhood if

$$d(I(x_1, y_1), H^{-1} \cdot I_{tran}(x_2, y_2)) < t. \quad (31)$$

Here  $H$  is the homography matrix between the original image  $I$  and its transformed version  $I_{tran}$  [45].

### C. Experimental Results

1) *Comparison of Gradient Maps*: In this experiment, the gradient maps generated from the original color images and the corresponding Bayer versions are compared. Note that for the INRIA dataset, gamma compression is applied to the converted Bayer pattern images to adjust the contrast, while this is not needed for the other two datasets.

The comparison results of different versions of gradient maps are presented in Table IV. Generally speaking, all the three evaluation criteria reveal similar trends that different versions of gradient maps are close to each other. As shown in Table IV, for the Kodak dataset, the gradients generated from color as well as Bayer pattern images are almost identical, while for the other two datasets, the similarities are slightly lower. This is because for the Kodak dataset, both the color and Bayer pattern images can be regarded as “true” (a true color image dataset with Bayer version generated by subsampling), while for the SHTech dataset and the PASCALRAW dataset, images are interpolated from Bayer pattern images using

TABLE V  
COMPARISON RESULTS OF BAYER IMAGE BASED AND COLOR IMAGE BASED BLUR AND RESIZE

Operation	Parameter		Average		
	Bayer	Color	MSSIM	MSE	PSNR
Gaussian blur	3×3 kernel	3×3 kernel	0.952	46.010	32.334
		5×5 kernel	0.979	18.040	36.293
		7×7 kernel	0.988	9.807	38.962
		9×9 kernel	0.985	11.762	38.094
Resize	Scale=0.5		0.938	70.453	30.232
	Scale=2		0.912	93.584	30.031
Blur & Resize	3x3 kernel, scale=0.5	7x7 kernel, scale=0.5	0.977	21.444	35.499
	3x3 kernel, scale=2	7x7 kernel, scale=2	0.976	15.667	36.691

demaicing algorithm. It is well known that extra errors will be introduced no matter how sophisticated the demosaicing algorithms is. This can be observed from the comparison results of the true color images and images generated using different demosaicing algorithms shown in Table II. Moreover, for the INRIA dataset, both the color and Bayer pattern images are “estimated” since the color version is interpolated and the Bayer version is reversely converted from the color version. Errors are injected in both forward and reverse ISP pipeline. Therefore, for the evaluation of the proposed Bayer pattern image-based gradient extraction pipeline, the Kodak dataset is more reliable than the other two. Note that as we mentioned, for the INRIA dataset, proper gamma compression is necessary. This can be illustrated using Fig. 7, where three versions of HOG descriptors, i.e., HOG from the original image, HOG from the Bayer pattern image without gamma compression and HOG from the Bayer pattern image with gamma compression, are presented. As shown in Fig. 7(f), the descriptors cannot find enough features in low contrast Bayer pattern image without gamma compression (in Fig. 7(b)). But after adjusting the contrast by gamma compression, the HOG feature extracted from Fig. 7(c) becomes more stable, and close to the one extracted from the original color image in Fig. 7(d).

2) *Blur and Resize*: In this work, the comparison of the blur and resize results are performed in the Bayer domain to reduce the impact of the ISP pipeline. For Bayer pattern images, blur and resize are directly applied on the super-pixel structure, while for color images, a resample operation is needed after blur and resize. The Kodak dataset is used in this experiment.

Presented in Table V are the comparison results of blur and resize. For a certain kernel,  $\sigma$  can be determined by the specific application or using the following equation [46]

$$\sigma = 0.3 \times ((length_k - 1) \times 0.5 - 1) + 0.8. \quad (32)$$

According to the experiment, blur and resize on Bayer pattern images using super-pixel structure generates similar results with that on color images. It can be observed from Table V that the 7×7 kernel for color images approach to the 3×3 kernel for super-pixel Bayer pattern images. This is because a super-pixel is a collection of pixels in a Bayer pattern which may expand the smooth area. The results in Table V reveal

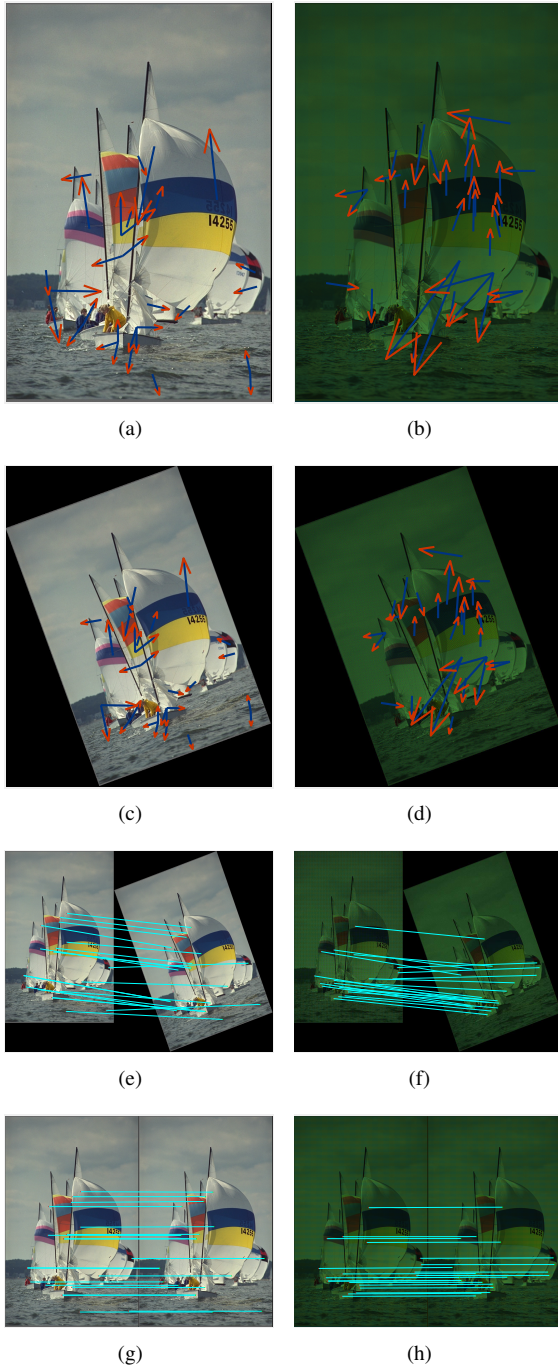


Fig. 8. (a)-(d): Part of the SIFT descriptors in the original Kodim09 image, its Bayer version and corresponding 20-degree-rotate version. (e)-(f): Twenty matches in (c) and (d). (g)-(h): Projecting the matches in (e) and (f) back to the location in (a) and (b) by homography matrix  $H$ .

that the Bayer pattern image-based blur and resize generates similar results to the color image-based operations.

3) *Key points matching*: Fig. 8 illustrates the key point matching performance based on SIFT feature using the original color version of Kodim09 image and its resampled Bayer version. As we can see, matched points can be identified in both color and Bayer pattern image pairs, meaning that the SIFT features extracted from the Bayer pattern images are robust regardless of the rotate operation.

To evaluate the scale and rotation invariance of the SIFT

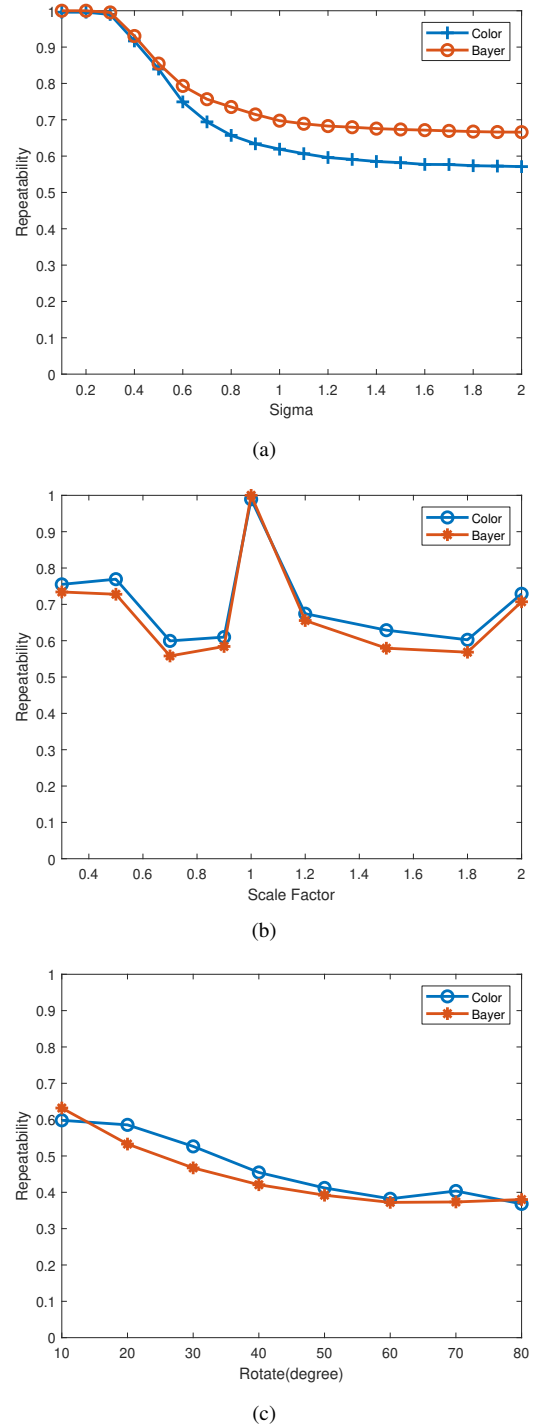


Fig. 9. Average repeatability of SIFT descriptor after (a) blur, (b) scale change and (c) rotate.

descriptor, the original images and the Bayer pattern images are transformed into different versions by blurring, scaling and rotating. The repeatability among each image is evaluated using the criteria mentioned in Section IV-B. Euclidean distance is used as the distance measurement between a pair of matching pixels. The parameter  $t$  in Equation (31) is set to 3.

Fig. 9 depicts the average repeatability scores for both color and Bayer version. As it can be observed, the curves in Fig. 9 are very close to each other, with the Bayer version performs

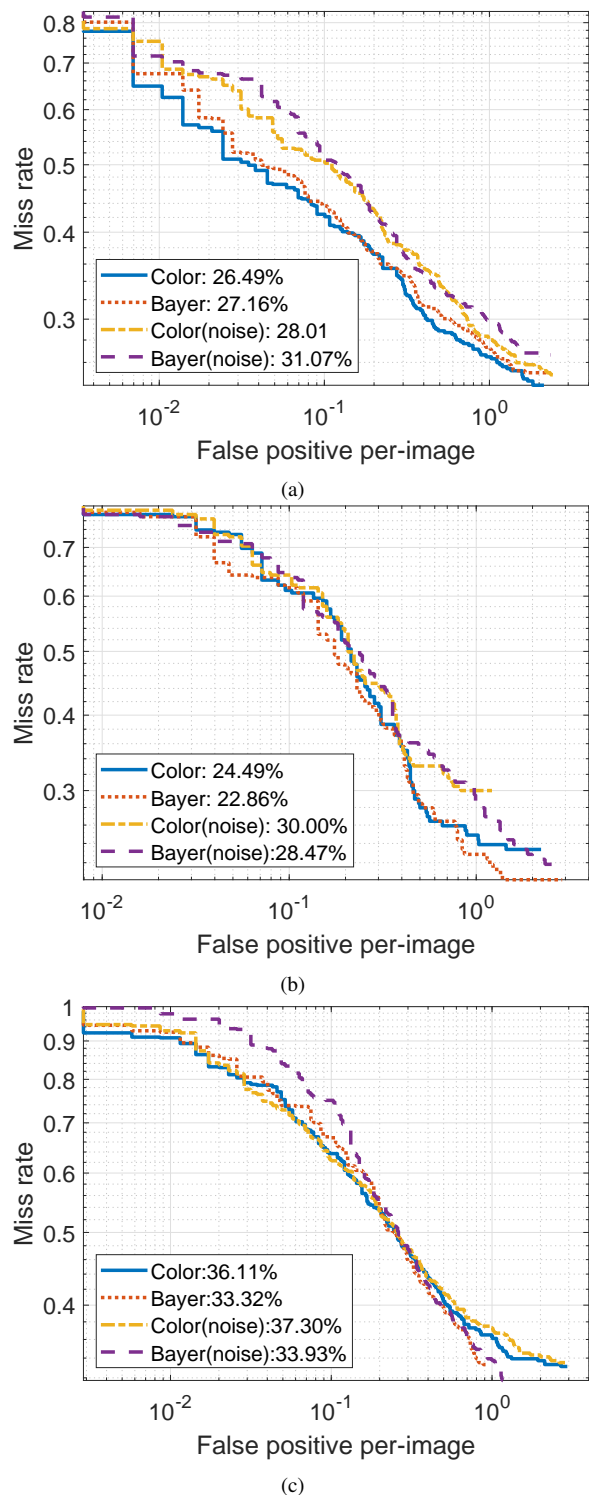


Fig. 10. Evaluation of pedestrian detection performance based on different versions of gradients using (a) the INRIA dataset, (b) the SHTech dataset and (c) the PASCALRAW dataset.

slightly better in the blur experiment and slightly worth in the scale and rotate experiment. But the performance differences are almost negligible.

4) *Pedestrian detection*: The HOG+SVM model is used as benchmark framework to evaluate the performance of the proposed Bayer pattern image-based gradients in object detection algorithms. For color and Bayer version datasets, the

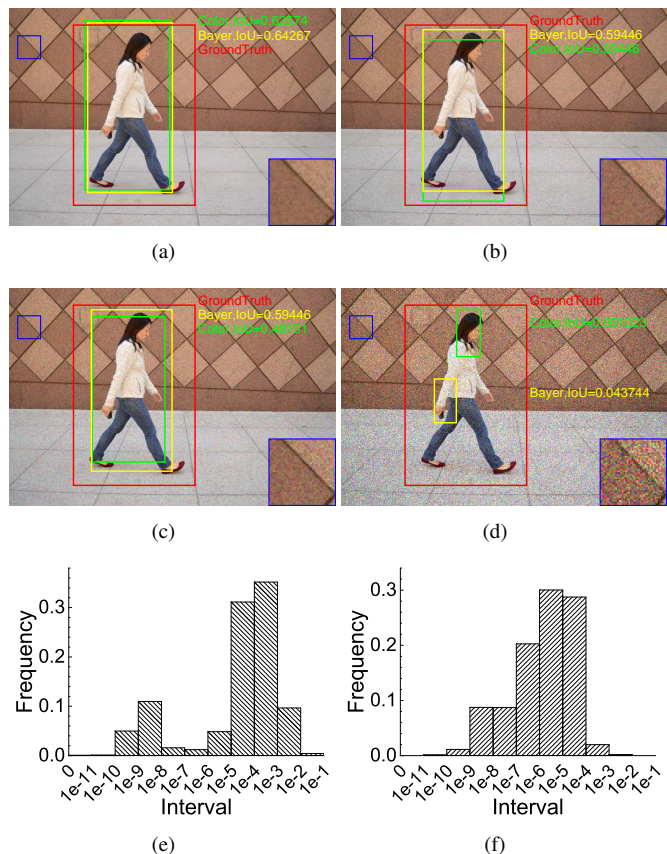


Fig. 11. The pedestrian detection results on (a) the original image, (b) noisy image with parameters of  $a = 9.63 \times 10^{-4}, b = 3.43 \times 10^{-5}$ , (c)  $a = 4.80 \times 10^{-3}, b = 2.00 \times 10^{-4}$ , (d)  $a = 3.59 \times 10^{-2}, b = 3.40 \times 10^{-3}$ . (e) The distribution of the estimated noise parameter  $a$  for the SID dataset. (f) The distribution of the estimated noise parameter  $b$  for the SID dataset.

model is trained on the corresponding dataset respectively. Fig. 10 shows the pedestrian detection results on INRIA, SHTech and PASCALRAW datasets. As we can see, the performances of detection rate versus false positive per image are very close for different versions of images. As shown in Fig. 10(a), HOG+SVM achieves 72.84% detection rate at 1 false positive-per image (FPPI) on Bayer version of the INRIA dataset, compared to a 73.51% detection rate at the same FPPI on the original INRIA dataset. The results are similar on the SHTech dataset, while the miss rate at 1 FPPI in SHTech dataset is slightly better than that in INRIA dataset for both Bayer and color version. This is due to the difference in the number and posture of the dataset samples. In PASCALRAW datasets, the detection rate for Bayer version is also close to its color version counterpart. Therefore, the gradients extracted directly from the Bayer pattern images are robust enough to be used in pedestrian detection algorithm, while the performance can be maintained.

The pedestrian detection performance under the influence of noise is also presented in Fig. 10. Note that in this experiment, the models are not retrained, i.e., the models trained using the noise-free images are used for pedestrian detection in noisy images. It can be found that the detection performance decreases slightly on all three datasets for both Bayer and color versions. The detection results on one of the images

with different noise level are shown in Fig. 11(a)-(d). It is found that with the increase of noise level, the bounding boxes tend to be smaller. As shown in Fig. 11(d), where the severest noise parameters are applied, the model seems not working for both Bayer and color versions. However, from the parameters distribution shown in Fig. 11(e) and (f), it can be found that such noise parameters ( $>0.01$ ) happens with a very small probability (less than 0.4%). The noise levels in most practical cases are similar to that in Fig. 11(b) and (c). Therefore, as we have seen in Fig. 10, the FPPI of noisy and noise-free datasets are very close to each other for both Bayer and color versions.

## V. DISCUSSION

The objective of computer vision is to obtain high-level understandings from images and videos. Traditional vision algorithms take fully rendered color images as inputs. However, in scenarios where color is not required, such as the gradient-based algorithms discussed in this paper, demosaicing is redundant. It not only costs computing time, but also wastes three times the storage space to get almost the same results.

It has been shown in [7] that in a conventional computer vision system consisting of an image sensor, an image signal processor and a vision processor (to run the computer vision algorithms), the image signal processor consumes a significant amount computation resources, processing time and power. For example, a well-designed deformable parts models (DPM) processor consumes only 58.6 mW to process 1080P videos at 30 frames per second (FPS), while a typical image signal processor dissipates around 250 mW to process videos with the same resolution and frame rate [47]. Therefore, from the system perspective, if we can skip the ISP pipeline (or most of the ISP steps), the computational complexity and power consumption of the computer vision system can be reduced significantly. Even in some features where color information is necessary, such as integral channel features (ICF) [48] or color descriptors in SIFT family [26], the location of demosaicing in the ISP pipeline need to be reconsidered. This is because as long as the mosaic structure is maintained, color information can be recovered whenever it is needed, through demosaicing for example. Moreover, though this paper shows that gradients extracted from Bayer pattern images are close to that from color images, the optimality of color image-based gradients extraction deserves a careful reconsideration.

## VI. CONCLUSION

In this paper, the impact of demosaicing on gradient extraction is studied and a gradient-based feature extraction pipeline based on raw Bayer pattern images is proposed. It is shown both theoretically and experimentally that the Bayer pattern images are applicable to the central difference gradient-based algorithms without performance degradation, or even with superior performance in some cases. The color difference constancy assumption, which is widely used in various demosaicing algorithms, is applied in the proposed Bayer pattern image-based gradient extraction pipeline. Experimental results show that the gradients extracted from Bayer pattern

images are robust enough to be used in HOG-based pedestrian detection algorithms and SIFT-based matching algorithms. Therefore, if gradient is the only information needed in a vision algorithm, the ISP pipeline (or most of the ISP steps) can be eliminated to reduced the computational complexity as well as power consumption of the systems.

## REFERENCES

- [1] O. Losson, L. Macaire, and Y. Yang, "Comparison of color demosaicing methods," *Advances in Imaging and Electron Physics*, vol. 162, pp. 173–265, 2010.
- [2] B. E. Bayer, "Color image filter." [Online]. Available: <https://patents.google.com/patent/US3971065A/en>. Accessed September 10, 2019.
- [3] R. Ramanath, W. E. Snyder, Y. Yoo, and M. S. Drew, "Color image processing pipeline," *IEEE Signal Processing Magazine*, vol. 22, no. 1, pp. 34–43, 2005.
- [4] F. Heide, M. Steinberger, Y. T. Tsai, M. Rouf, D. Pająk, D. Reddy, O. Gallo, J. Liu, W. Heidrich, K. Egiazarian, *et al.*, "Flexisp: A flexible camera image processing framework," *ACM Transactions on Graphics*, vol. 33, no. 6, pp. 231:1–231:13, 2014.
- [5] J. Sporing and J. Weickert, "Information measures in scale-spaces," *IEEE Transactions on Information Theory*, vol. 45, no. 3, pp. 1051–1058, 1999.
- [6] A. Omid-Zohoor, C. Young, D. Ta, and B. Murmann, "Toward always-on mobile object detection: Energy versus performance tradeoffs for embedded hog feature extraction," *IEEE Transactions on Circuits and Systems for Video Technology*, vol. 28, pp. 1102–1115, May 2018.
- [7] M. Buckler, S. Jayasuriya, and A. Sampson, "Reconfiguring the imaging pipeline for computer vision," in *Proc. IEEE International Conference on Computer Vision*, pp. 975–984, 2017.
- [8] H. Blasinski, J. Farrell, T. Lian, Z. Liu, and B. Wandell, "Optimizing image acquisition systems for autonomous driving," *Electronic Imaging*, vol. 2018, pp. 1–7, Jan 2018.
- [9] Z. Y. Liu, L. Trisha, F. Joyce, and W. Brian, "Neural network generalization: The impact of camera parameters," *arXiv*, 2019.
- [10] O. Losson and L. Macaire, "CFA local binary patterns for fast illuminant-invariant color texture classification," *Journal of Real-Time Image Processing*, vol. 10, no. 2, pp. 387–401, 2015.
- [11] A. Aberkane, O. Losson, and L. Macaire, "Edge detection from bayer color filter array image," *Journal of Electronic Imaging*, vol. 27, no. 1, pp. 53–66, 2018.
- [12] O. Losson, A. Porebski, N. Vandenbroucke, and L. Macaire, "Color texture analysis using CFA chromatic co-occurrence matrices," *Computer Vision and Image Understanding*, vol. 117, no. 7, pp. 747–763, 2013.
- [13] A. Trifan and A. J. Neves, "On the use of feature descriptors on raw image data," in *Proc. International Conference on Pattern Recognition Applications and Methods*, pp. 655–662, 2016.
- [14] A. J. Neves, A. Trifan, B. Cunha, and J. L. Azevedo, "Real-time color coded object detection using a modular computer vision library," *Advances in Computer Science: an International Journal*, vol. 5, no. 1, pp. 110–123, 2016.
- [15] H. Can and M. Brown, "A software platform for manipulating the camera imaging pipeline," in *European Conference on Computer Vision*, vol. 9905, pp. 429–444, Oct 2016.
- [16] R. Ramanath, W. E. Snyder, and G. L. Billbro, "Demosaicking methods for bayer color arrays," *Journal of Electronic Imaging*, vol. 11, no. 3, pp. 306–315, 2002.
- [17] L. Wenmiao and T. Yap-Peng, "Color filter array demosaicking: new method and performance measures," *IEEE Transactions on Image Processing*, vol. 12, no. 10, pp. 1194–1210, 2003.
- [18] R. Kimmel, "Demosaicing: image reconstruction from color CCD samples," *IEEE Transactions on Image Processing*, vol. 8, no. 9, pp. 1221–1228, 1999.
- [19] B. K. Gunturk, Y. Altunbasak, and R. M. Mersereau, "Color plane interpolation using alternating projections," *IEEE Transactions on Image Processing*, vol. 11, no. 9, pp. 997–1013, 2002.
- [20] P. Eliason, L. Soderblom, and P. Chavez Jr, "Extraction of topographic and spectral albedo information from multispectral images," *Photogrammetric Engineering and Remote Sensing*, vol. 47, pp. 1571–1579, Oct 1981.
- [21] P. A. Viola and M. J. Jones, "Rapid object detection using a boosted cascade of simple features," in *Proc. IEEE Computer Society Conference on Computer Vision & Pattern Recognition*, 2003.

- [22] T. Ojala, M. Pietik inen, and T. M enp en, “Gray scale and rotation invariant texture classification with local binary patterns,” in *Proc. European Conference on Computer Vision*, vol. 1842, pp. 404–420, Jun 2000.
- [23] D. G. Lowe, “Distinctive image features from scale-invariant keypoints,” *International Journal of Computer Vision*, vol. 60, no. 2, pp. 91–110, 2004.
- [24] N. Dalal and B. Triggs, “Histograms of oriented gradients for human detection,” in *Proc. IEEE Conference on Computer Vision and Pattern Recognition*, pp. 886–893.
- [25] H. Bay, T. Tuytelaars, and L. Van Gool, “Surf: Speeded up robust features,” in *Proc. Computer Vision and Image Understanding*, vol. 110, pp. 404–417, Jun 2006.
- [26] K. Van De Sande, T. Gevers, and C. Snoek, “Evaluating color descriptors for object and scene recognition,” *IEEE Transactions on Pattern Analysis and Machine Intelligence*, vol. 32, no. 9, pp. 1582–1596, 2009.
- [27] Y. G. Morel J M, “ASIFT: A new framework for fully affine invariant image comparison,” *SIAM Journal on Imaging Sciences*, vol. 2, no. 2, pp. 438–469, 2009.
- [28] P. F. Felzenszwalb, R. B. Girshick, D. McAllester, and D. Ramanan, “Object detection with discriminatively trained part-based models,” *IEEE Transactions on Pattern Analysis and Machine Intelligence*, vol. 32, no. 9, pp. 1627–1645, 2009.
- [29] D. G. Lowe, “Object recognition from local scale-invariant features,” in *Proc. IEEE International Conference on Computer Vision*, vol. 99, pp. 1150–1157, 1999.
- [30] R. C. Gonzalez and P. Wintz, “Digital image processing,” *Reading, Mass., Addison-Wesley Publishing Co., Inc. (Applied Mathematics and Computation)*, 1977.
- [31] J. E. Adams, “Design of practical color filter array interpolation algorithms for digital cameras,” *The International Society for Optical Engineering*, vol. 117, no. 7, pp. 117–125, 1997.
- [32] R. Lukac, *Single-Sensor Imaging: Methods and Applications for Digital Cameras (1st. ed.)*. USA: CRC Press, Inc., 2008.
- [33] R. W. Franzen, “True color kodak images.” [Online]. Available:<http://r0k.us/graphics/kodak/>. Accessed September 10, 2019.
- [34] Jerpelea, “FreeDcam.” [Online]. Available:<https://github.com/freexperia/FreeDcam>. Accessed September 10, 2019.
- [35] A. Omid-Zohoor, D. Ta, and B. Murmann, “PASCALRAW: Raw image database for object detection.” [Online]. Available:<http://purl.stanford.edu/hq050zr7488>. Accessed September 11, 2019.
- [36] “Inria person dataset.” [Online]. Available:<http://pascal.inrialpes.fr/data/human/>. Accessed September 10, 2019.
- [37] C. Chen, C. Qifeng, X. Jia, and K. Vladlen, “Learning to see in the dark,” in *Proc. the IEEE International Conference on Computer Vision*, May 2018.
- [38] W. F. Xue, L. Zhang, X. Q. Mou, and C. Alan, “Gradient magnitude similarity deviation: A highly efficient perceptual image quality index,” *IEEE Transactions on Image Processing*, vol. 23, no. 2, pp. 684–695, 2014.
- [39] S. Welstead, *Fractal and Wavelet Image Compression Techniques*. Society of Photo-Optical Instrumentation Engineers, Jan 1999.
- [40] Z. Wang, A. C. Bovik, H. R. Sheikh, E. P. Simoncelli, *et al.*, “Image quality assessment: from error visibility to structural similarity,” *IEEE Transactions on Image Processing*, vol. 13, no. 4, pp. 600–612, 2004.
- [41] F. Alessandro, T. Mejdj, K. Vladimir, and E. Karen, “Practical poissonian-gaussian noise modeling and fitting for single-image raw-data,” *IEEE Transactions on Image Processing*, vol. 17, no. 10, pp. 1737–1754, 2008.
- [42] L. Mykhail, V. Benoit, V. L. Vladimir, and C. Kacem, “Image informative maps for component-wise estimating parameters of signal-dependent noise,” *Journal of Electronic Imaging*, vol. 22, no. 1, 2013.
- [43] P. Dollar, C. Wojek, B. Schiele, and P. Perona, “Pedestrian detection: A benchmark,” in *Proc. IEEE Computer Society Conference on Computer Vision & Pattern Recognition*, pp. 304–311, Jun 2009.
- [44] C. Schmid, R. Mohr, and C. Bauckhage, “Evaluation of interest point detectors,” *International Journal of computer vision*, vol. 37, no. 2, pp. 151–172, 2000.
- [45] K. Mikolajczyk and C. Schmid, “A performance evaluation of local descriptors,” *IEEE Transactions on Pattern Analysis & Machine Intelligence*, vol. 27, no. 10, pp. 1615–1630, 2005.
- [46] “OpenCV 2.4.13.7 documentation.” [Online]. Available:<https://docs.opencv.org/2.4/modules/imgproc/doc/filtering.html#getgaussiankernel>. Accessed September 11, 2019.
- [47] A. Suleiman, Z. Zhang, and V. Sze, “A 58.6 mw 30 frames/s real-time programmable multiobject detection accelerator with deformable parts models on full hd 1920x1080 videos,” *IEEE Journal of Solid-State Circuits*, vol. 844–855, pp. 1–12, Mar 2017.
- [48] P. Dollar, Z. Tu, P. Perona, and S. Belongie, “Integral channel features,” in *Proc. British Machine Vision Conference*, pp. 91.1–91.11, 2009.